Agricultural and Forest Meteorology 338 (2023) 109429

Contents lists available at ScienceDirect

Agricultural and Forest Meteorology

journal homepage: www.elsevier.com/locate/agrformet

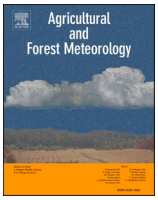

Using just a canopy height model to obtain lidar-level accuracy in 3D forest canopy shortwave transmissivity estimates

Clare Webster [a,b,c,*], Richard Essery [d], Giulia Mazzotti [b,e], Tobias Jonas [b]

[a] Department of Geosciences, University of Oslo, Oslo, Norway
[b] WSL Institute for Snow and Avalanche Research SLF, Davos Dorf, Switzerland
[c] Swiss Federal Institute for Forest, Snow and Landscape Research WSL, Birmensdorf, Switzerland
[d] School of Geosciences, University of Edinburgh, Edinburgh, United Kingdom
[e] Univ. Grenoble Alpes, Université de Toulouse, Météo-France, CNRS, CNRM, Centre d'Études de la Neige, Grenoble, France

ARTICLE INFO

Keywords:
Shortwave radiation modelling
Radiation transfer
Canopy height model
Airborne lidar
Hemispherical photography
Synthetic hemispheric images

ABSTRACT

This study presents a new model for calculating canopy shortwave radiation transmissivity from synthetic hemispheric images using only information contained within a canopy height model (CHM) – CanopyHeightModel2Radiation (C2R). The enhanced version calculates synthetic hemispherical images based on the geometric arrangement of the surrounding canopy while applying a statistical correction for canopy transmissivity using canopy thickness and tree species leaf area. The simple input data and statistical correction make this model suitable for estimating canopy transmissivity across large spatial extents typical of land surface models for which canopy transmissivity or radiation is a primary input variable. Performance of C2R-enhanced is assessed against hemispherical photographs, and compared to a basic version of C2R without transmissivity correction, and two versions of a Lidar2Radiation model (L2R-enhanced, L2R-basic) with either a basic representation of canopy structure or an enhanced representation including trunks and branches within tree crowns. The two enhanced models (L2R-enhanced and C2R-enhanced) perform best compared to hemispherical photographs, while the L2R-basic and C2R-basic models over- and underestimate canopy transmissivity, respectively. At 1-meter and 10-minute resolution, the two enhanced models perform similarly, but exact timing and location of transmissivity controlled by canopy structure is better represented in the physically explicit L2R-enhanced model. Across hourly and 25 × 25 m grid-averaged scales, both enhanced models achieve similar estimates of canopy transmissivity. Based on these results, it is recommended that the purely physically-based representation in the L2R-enhanced model is used when estimates of canopy transmissivity at high spatial and temporal (meter and minute) resolutions are necessary, while the computationally more efficient C2R-enhanced model is used when calculating canopy transmissivity within spatially aggregated grid cells, for example, as input into coarser-resolution land surface models. Incorporating C2R-enhanced into existing forest energy balance models creates exciting opportunities for investigating forest structure changes on forest hydrology and ecosystems across previously impossible spatial extents.

1. Introduction

Shortwave radiation is a main driver of key forest processes such as evapotranspiration, snowmelt, photosynthesis, and biodiversity (Baldocchi et al., 2000; Bales et al., 2011; Hardy et al., 2004; Zellweger et al., 2020), and a required input in many physically-based land surface models used to understand and predict these processes. Distributed measurements of sub-canopy shortwave radiation show substantial variabilities over meter and minute scales due to the complex interaction between 3D forest structure and shifting solar position (Malle et al., 2019; Mazzotti et al., 2019). Incorporating forest processes at these scales has been shown to be important for predicting the forest energy balance at coarser model resolutions (Mazzotti et al., 2021; Broxton et al., 2021), requiring datasets and modelling methods that represent tree-scale solar radiation interactions over scales typically covered by land surface models (i.e. > 100 km^2).

Total sub-canopy shortwave radiation is determined by the sum of the direct and diffuse components. The diffuse component can be

* Corresponding author.
E-mail address: clare.webster@geo.uio.no (C. Webster).

https://doi.org/10.1016/j.agrformet.2023.109429
Received 7 July 2022; Received in revised form 9 March 2023; Accepted 18 March 2023
Available online 20 May 2023

described by the sky-view fraction (also referred to as diffuse transmissivity), which is static in time but not space. The direct component is described by the transmissivity of the canopy in the path of the solar beam (time-varying direct-beam transmissivity) and varies both in space and time as the sun moves along the solar track. At point scales, these two variables can be very accurately estimated by hemispherical photography and associated analysis methods (Musselman et al. 2012a, b; Jonas et al., 2020). Hemispherical photography, however, is only suitable for small, forested sites (< 100 m^2) and is not suitable for modelling ecohydrological processes across relevant landscapes.

The increasing availability of remotely sensed forest structure datasets now means spatially distributed methods for estimating sub-canopy shortwave radiation are being developed. The most common of these datasets is airborne lidar data, which has been used with voxel-based ray-trace models (e.g. Musselman et al., 2013; Kükenbrink et al., 2021), GIS-based shortwave radiation models (e.g. Bode et al., 2014), and hemispherical image-based ray-trace models (e.g. Webster et al., 2020). These models accurately calculate canopy transmissivity maps at meter and minute resolutions by directly accounting for detailed and realistic three-dimensional canopy structure. For example, the ray-trace model in Musselman et al. (2013) represented a much higher level of stand-scale variability in shortwave transmission compared to a simple Beer's-type model that used leaf area index (LAI), and particularly captured those patterns associated with individual trees. At the meter and minute scale, Webster et al., (2020) demonstrated estimates of sub-canopy shortwave radiation could be improved through augmentation of airborne lidar data, specifically by adding further stem and branch elements which are typically underrepresented in raw point cloud data acquired from above the canopy. Comparison between real and synthetic hemispherical images demonstrated that the enhanced lidar better represented individual tree structure compared to the basic point cloud, and corresponding sub-canopy shortwave radiation estimates better matched with radiometer measurements.

As an important application of these shortwave radiation modelling methods, detailed estimates of canopy transmissivity can now be included in spatially distributed physically-based forest energy balance models. For example, Mazzotti et al. (2020) used hemispherical photographs and the radiation model HPEval from Jonas et al. (2020) as input for point simulations with the forest snow model FSM2. They showed significant improvement in snowmelt estimates by FSM using explicit time-varying direct-beam transmissivity and sky-view fraction compared to a simpler model version that uses LAI and canopy height as the only canopy descriptors, thus demonstrating the value of using a hemispherical image-based radiative transfer model framework for fully distributed hyper-resolution forest energy balance (< 5 m) simulations.

Hyper-resolution spatially distributed physically-based models (e.g. Mazzotti et al., 2020; Broxton et al., 2015) are valuable not only through their contribution to understanding meter-scale variabilities in forest energy exchange processes and how these change across heterogeneous landscapes, but also through their representation of the sub-grid variability of coarser resolution models (Mazzotti et al., 2021; Broxton et al., 2021). This sub-grid representation can facilitate assessment of coarser resolution model performance, particularly in how well complex processes that vary at the sub-grid scale are represented at the coarser resolutions. For example, Mazzotti et al. (2021) used hyper-resolution (2-meter, 2 minute) output from the Webster et al. (2020) synthetic hemispherical image-based radiation transfer model and averaged estimates of sky-view fraction and time-varying transmissivity to 50 m x 50 m grid cells and hourly time steps. Using these averaged transmissivity estimates as input to their snow model provided considerable improvements in estimates of grid-averaged snow mass and snow depletion compared to the model version that describes canopy structure using grid averaged values of LAI and canopy height.

The representation of canopy structure using LAI and canopy height closely resembles what is currently included in commonly used forest snow schemes of coarse-resolution land surface models such as CLM, CLASS and SUMMA (Lawrence et al., 2019; Bartlett et al.. 2006; Clark et al., 2015). Explicit representation of fine-scale canopy structure, and subsequently, accurate estimates of grid-averaged canopy transmissivity are therefore an important step to explicitly represent forest structural controls on sub-canopy incoming shortwave radiation at model resolutions coarser than the spatial scale of its true variability (Broxton et al., 2021). Providing grid averaged sky-view fraction and time-varying transmissivity values as model input is a potential solution to incorporate the complex process of solar radiation transmission in intermediate- to coarse-resolution models (Mazzotti et al., 2021). Improvement in the representation of radiation transfer within these coarser-resolution models could make them more attractive for research applications such as snow hydrology, biodiversity and forest microclimate, and forest change impact studies. A problem, however, remains how to obtain hyper-resolution estimates required to arrive at accurate grid averaged transmissivities across the large spatial extents at which coarse-resolution models typically operate (i.e. over entire watersheds, mountain ranges or continents).

The fact that a simple grid-averaged canopy transmissivity can be used as input into these coarser resolution models implies that output from a physically explicit hyper-resolution shortwave transmission model (accurate to meter and minute scales) is not necessarily a requirement should a simpler and more efficient model be able to arrive at similarly accurate estimates of grid-averaged shortwave transmissivity. Physically explicit transmissivity models typically require high resolution lidar data as input to represent tree crown position, shape and densities when calculating shortwave radiation transmission through the canopy. The limitation of these models is that high resolution lidar datasets capable of representing the required level of detail within tree crowns ($>$ 20-30 pts/m^2) are typically only available across catchments in a best-case scenario (e.g. Currier et al., 2019). In general, datasets with this level of detail are not available across regions and/or mountain ranges (> 100 km^2) that are relevant for coarser resolution modelling. Finally, the computational intensity and memory requirements of such a spatially explicit hyper-resolution model means they are simply unsuitable for modelling shortwave transmission across land surface model domains.

Instead, a more computationally simple model that can represent the average conditions across a grid cell will be sufficient for calculating shortwave transmission input to land surface models. To this end, we present the model CanopyHeightModel2Radiation (C2R), a hemispherical-based shortwave transmissivity model that uses just a canopy height model (CHM) to represent canopy structure, instead of high resolution airborne lidar point clouds. CHMs can be calculated using airborne lidar data that is much lower in resolution than those datasets required to run spatially explicit hyper-resolution shortwave transmissivity models, and are typically available over regions larger than 100 km^2 (e.g. 0.5-15 pts/m^2; Ferraz et al., 2018; Swisstopo, 2017; National Land Survey of Finland, 2019). Additionally, CHMs can be calculated using other data acquisition methods such as stereo imagery from remotely piloted and piloted aircraft and satellites (Mohan et al., 2017; Ginzler and Hobi, 2015; Piermattei et al., 2018). Importantly, CHMs are more widely available than high resolution lidar data. Catchment and nationwide lidar datasets typically have a minimum point density of 1-2 pts/m^2, which can be sufficient to calculate a CHM that resolves individual tree crowns. Given that CHMs have the potential to cover much greater spatial extents than high resolution lidar, they are more suited for large-scale model applications.

The simple data requirements of only a CHM and knowledge of tree species or type makes it suitable to apply across large spatial domains where detailed hyper-resolution 3D canopy structure datasets are unavailable and currently unobtainable. The aim of the C2R model is to increase the extent of model domains, as well as regions across which detailed estimates of canopy shortwave radiation transmissivity can be obtained and physically-based energy balance estimates of canopy processes can be improved.

We assess the performance of C2R with other existing hemispherical-based radiation model approaches using real hemispherical photographs (Jonas et al. 2020), basic and enhanced airborne lidar (Webster et al., 2020) and a basic (tree position only) and enhanced (statistical correction) version of the C2R model presented here. We first compare hyper-resolution (1 meter and minute-scale) from the 5 models, and then compare estimates at 25 × 25 m grid cells at hourly resolution from the lidar and chm enhanced models. The results from the model comparisons should be used to inform shortwave transmission model choice for various physically-based energy balance modelling applications within forests.

2. Site description and data

2.1. Site description

The model domain in the eastern Swiss Alps (Fig. 1) is the same as that used by Webster et al. (2020) and Mazzotti et al. (2021). The forest within the model domain is discontinuous in structure and predominantly Norway Spruce with a small number of isolated individual Larch trees. Discontinuous forest structure, wide variation in sky-view fraction, range of forest gap sizes and minimal buildings or other manmade infrastructure make this an ideal site to assess shortwave radiation and forest energy balance model performance. Mean and maximum tree-height across the study area are 28 m and 44 m, respectively. This area was chosen due to the availability of real hemispherical photographs and spatially coincident radiometer measurements that have been previously used for assessing the performance of the radiative transfer model in Webster et al. (2020) and model upscaling strategies of FSM2 (Mazzotti et al. 2021). Hemispherical photographs used for validation in this study were collected during the 2018 and 2019 snow seasons and aerial imagery over the domain was collected in March 2019.

2.2. Canopy data

Airborne lidar data used in this study was first used by Moeser et al. (2014) and has been used in subsequent studies in the area by Webster et al. (2020) and Mazzotti et al. (2021). The data was acquired using a Riegl LMS Q560 mounted on a helicopter operating 700 m above ground. The wavelength was 1550 nm with pulse durations of 5 ns, and up to 7 returns per pulse. The maximum scan angle was ±15°. Lidar data covering the model domain has an average point density of 42 pts/m^2. The aerial survey was carried out in September 2010 with minimal forest structural change occurring in the 8-9 years between lidar data acquisition and manual validation measurements. Some tree removal in the center of one of the forest gaps, however, was identified when comparing the lidar data to the more recent aerial images. A canopy height model (CHM) at 0.5 m resolution was calculated from the lidar data using the methods described in Khosravipour et al. (2014).

3. Model description

3.1. Canopy Height Model to Radiation (C2R) model

C2R combines concepts introduced in Zellweger et al. (2019), Webster et al. (2020), Broxton et al. (2015) and Essery et al. (2008a). Creating synthetic hemispherical images from a CHM calculates the top of canopy horizon line (CHL; Fig. 2c). The horizon line tracing method was originally developed in Zellweger et al. (2019) and Webster et al. (2020) and used to include terrain in their synthetic images. The zenith angle of the horizon line is calculated at each 1° azimuth increment using a digital terrain model but when applied to a CHM instead of a terrain model it is physically explicit in its representation of tree position relative to the solar path. However, calculating a synthetic hemispherical image by treating the canopy as terrain would lead to underestimates sky-view fraction (V_f; diffuse transmissivity) and time-varying direct beam transmissivity (τ_{dir}) since trees are not 100% opaque bodies and light penetrates the canopy below the CHL. Broxton et al. (2015) accounted for this by applying a Beer's Law attenuation factor when the sun is below the CHL. The C2R model uses a more physical representation of canopy structure from the CHM to account for tree crown transmissivity by applying a statistical correction based on canopy thickness (calculated from the CHM) and tree species-specific

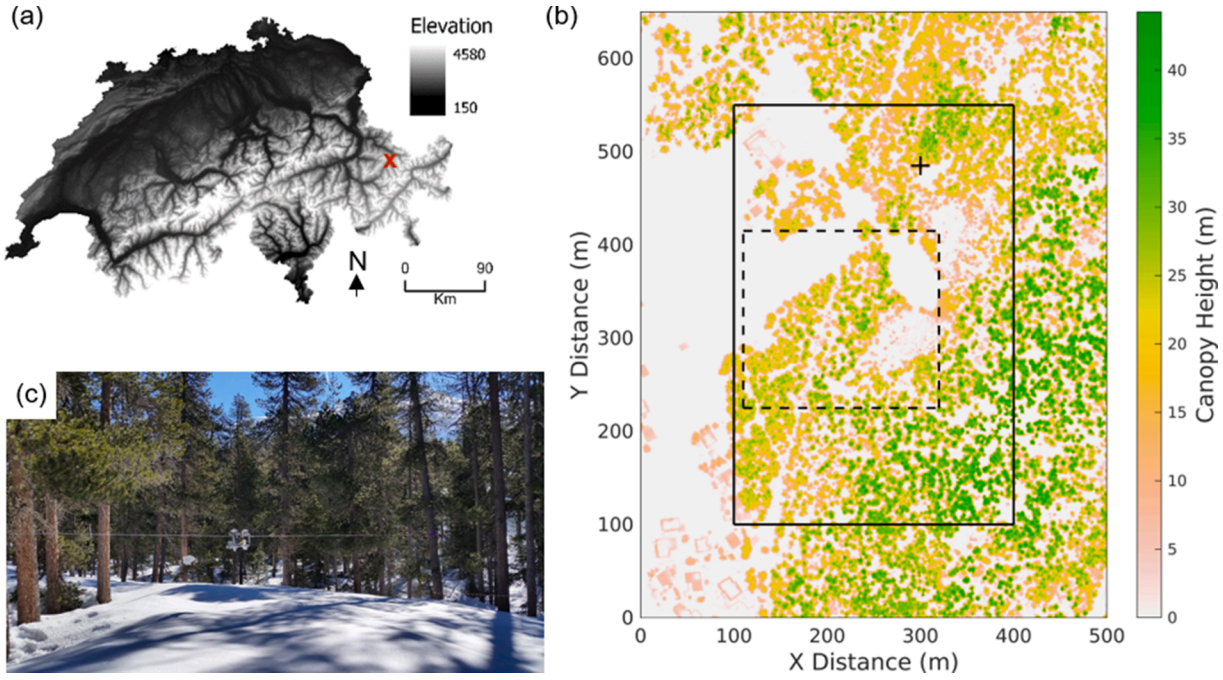

Fig. 1. (a) location of model domain (X) within Swiss Alps; (b) canopy structure within and surrounding the model domain (300 × 450m; solid line), area shown in aerial images (200 × 200m; dashed line) and approximate location of real hemispherical photographs I and II in Fig. 5 (+); (c) typical canopy structure and radiation transfer in the model domain.

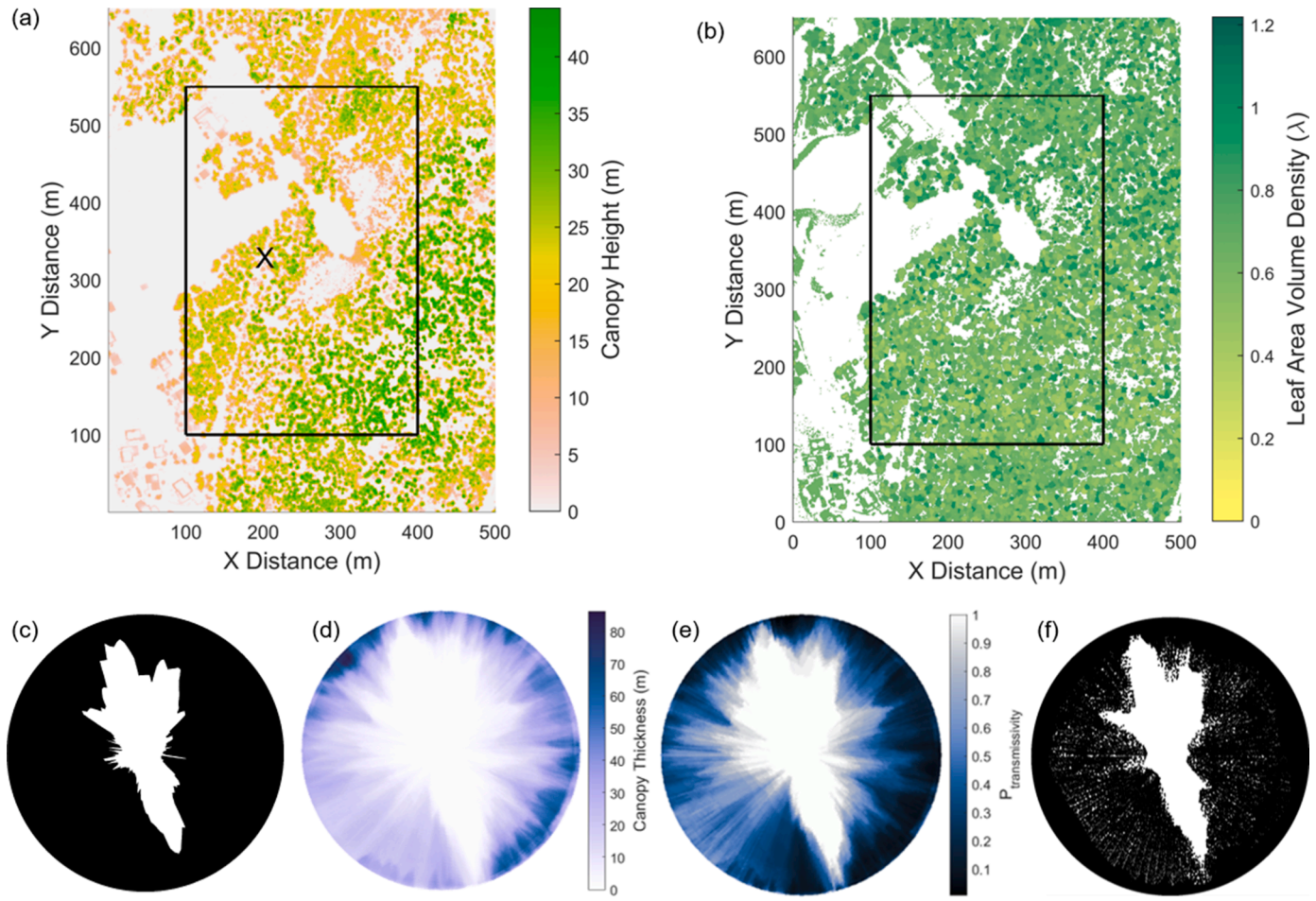

Fig. 2. (a) Canopy height model across model domain and surrounding 100 m; (b) leaf area volume density map across the same area in (a); (c) traced canopy horizon line from X in (a); (d) calculated canopy thickness across all zenith and azimuth angles up to 100m distance; (e) probability of direct beam transmissivity across the hemispherical view; (f) final synthetic hemispherical image at X.

leaf area that returns a probability of shortwave radiation transmission (Price, 1997; Essery et al., 2008a). This correction accounts for the fact that forest canopies and individual tree crowns are discontinuous structures and direct beam transmissivity can be high even when the solar position is below the calculated CHL.

The correction based on canopy thickness from Essery et al. (2008a) and Price (1997) uses the statistical model from Nilson (1971) that calculates the probability of light passing through the canopy based on path length and foliage area volume density of the canopy:

$$p_t = exp\left[- G(\theta) \sum \lambda l_t \right] \quad (1)$$

where G is a projection function that determines the foliage orientation, θ is the solar elevation, λ is the effective foliage area volume density, which is summed over all crowns that the path intersects (l_t). As in Essery et al. (2008a), we assumed a random foliage orientation (G = 0.5).

λ of each tree crown is calculated by dividing the leaf area (LA) by the crown volume (see equation 9 in Essery et al. 2008a). Both variables could be calculated using airborne lidar data, but since this model is aimed for large scale application and computational efficiency where high resolution airborne lidar is unavailable, we use an allometric equation to calculate leaf area and combine individual tree crown information from the CHM with an assumption of tree crown shape. LA of the trees in the study area is calculated using values for Norway Spruce from Goude et al. (2019):

$$\log(LA) = -8.31 + 2.61\log(DBH) - 0.07h \quad (2)$$

where DBH is trunk diameter at breast height and h is tree crown height. DBH is calculated using an allometric equation calculated by Jucker et al., 2017, who derived equations from a global database of > 100,000 measurements of stem diameter, height and crown diameter. We used the equation for temperate palearctic coniferous gymnosperm (biome '19' in their study).

Tree height and crown dimensions are calculated using the tree segmentation python implementation PyCrown (Zörner et al. 2018), based on the delineation algorithms from Dalponte and Coomes (2016). A simple paraboloid crown shape is assumed for all trees. Combining the generic paraboloid shape and tree crown statistics, λ is calculated for each tree crown using:

$$\lambda = \frac{LA}{0.5\pi r^2 (h - b)} \quad (3)$$

where r is the average radius of the segmented tree crown (tree crowns are not perfect circles) and (h - b) is the height of the tree above the base (b) of the tree crown. Across the study area, we assume a canopy base height of 2 m. An individual value λ is calculated for each tree crown, resulting in a map of λ across the study area (Fig. 2b).

Total path length (Σl_t) is determined by calculating canopy thickness across the hemispherical view in each 1° azimuth and zenith angle increments up to a maximum distance of 100m (Fig. 2d). At the same time, Σλ is calculated from the λ maps. Canopy thickness and total λ across the

hemisphere are then used in Eq. 1 to determine the probability of direct beam shortwave radiation transfer (p_t, Fig. 2e). Finally, the hemispherical images are binarized by generating a matrix of uniformly distributed random numbers (R) between 0 and 1, with the same number of pixels as the hemispherical images. Where p_t exceeds R, the transmissivity of the pixel is 1, and vice versa:

$$\tau = \begin{cases} 1 & p_t \geq R \\ 0 & p_t < R \end{cases} \quad (4)$$

resulting in a binarized hemispherical image (Fig. 2f). This binarization method was chosen to produce random gaps within the canopy to better replicate the natural forest structure. In many cases, the thinness of the top of individual trees (usually only one 0.5m pixel in the CHM) means p_t is close to 1. To better replicate the tops of tree crowns in the synthetic images, the points from the canopy height model (i.e. 0.5 m grid points of the top of the canopy) are also included in the synthetic images by converting the points to hemispherical coordinates as in Moeser et al. (2014) and Webster et al. (2020).

Local and regional terrain are also included in the image following the methods described in Webster et al. (2020) using 2 m and 25 m digital terrain models within a 300 m and 10 km radius around each image location, respectively. The high resolution terrain was included to represent local terrain variability between model points, while the medium resolution terrain was used to represent the topographic horizon line of the surrounding alpine region. Different terrain model resolutions and search radii were selected to optimize computational efficiency.

3.2. Shortwave radiation transmission

The calculated binarized hemispherical images are used with the shortwave radiation model from Jonas et al. (2020) and Webster et al. (2020). Jonas et al. (2020) developed the model for high temporal resolution estimates of sub-canopy incoming radiation using real hemispherical photographs. V_f is calculated following the methods described in Essery et al. (2008b). Calculations of τ_{dir} follow those in Jonas et al. (2020), which determines the proportion of canopy and sky pixels in the region of the calculated solar position in the image for each 2-minute time step. The 2-minute time step yields a spatially and temporally continuous sun track in the images combined with the 0.53° apparent diameter of the sun. The solar position was calculated using the NOAA parametrization (NOAA, 2005), resulting in a local azimuth and zenith angle for each hemispherical image and time step.

Maximum potential incoming direct and diffuse radiation in the forest (SW_{for}) were calculated by multiplying the above-canopy components by the direct and diffuse canopy transmissivity:

$$SW_{for} = SW_{dif}.V_f + SW_{dir}.\tau_{dir} \quad (5)$$

The partitioning scheme from Erbs et al. (1982) divides the above canopy maximum total incoming shortwave radiation (SW_{tot}) into the direct (SW_{dir}) and diffuse (SW_{dif}) components:

$$\frac{SW_{dif}}{SW_{total}} = \begin{cases} 1 - 0.09\tau_{atm} & \text{for } \tau_{atm} \leq 0.22 \\ 0.95 - 0.16\tau_{atm} + 4.39\tau_{atm}^2 - 16.64\tau_{atm}^3 + 12.34\tau_{atm}^4 & \text{for } 0.22 < \tau_{atm} \leq 0.8 \\ 0.165 & \text{for } 0.8 < \tau_{atm} \end{cases} \quad (6)$$

which describes the fraction of diffuse radiation in terms of the atmospheric transmissivity:

$$\tau_{atm} = \frac{SW_{tot}}{I_0.cos(\theta)} \quad (7)$$

where θ is the solar zenith angle, and I_o = 1367 W m^{-2} is used as the solar constant. In this study, the atmospheric transmissivity was assumed to be 1, thereby calculating the maximum possible radiation reaching the top of the canopy and subsequently transmitted to ground level. This removed the influence of weather conditions on assessing model performance. We selected this value to allow direct comparison between the models' representations of forest structure throughout the annual seasonal cycle. Note that if atmospheric transmissivity or above-canopy total shortwave radiation data were available, real sub-canopy shortwave radiation could be calculated using V_f and τ_{dir}, which was the method used by Jonas et al. (2020) and Webster et al. (2020) in their validation of the radiation model.

Jonas et al. (2020) performed statistical validation of their radiation model against measured sub-canopy shortwave radiation at 1 hour and 10 minute resolutions and calculated root mean square errors (RMSEs) of 17 and 28 W m^{-2}, respectively. Webster et al. (2020) used the same model on synthetic hemispherical images calculated from enhanced lidar data and obtained RMSEs of 28.7 and 59.3 W m^{-2} compared to sub-canopy measurements at two sites. These reported model errors are all within the measurement uncertainty of the radiometers used in those studies; therefore, we do not further assess the performance of the radiation model against measured values in this study.

3.3. Model implementation and validation

Synthetic hemispherical images were created at 10^5 point locations within the model domain at 1 m spacing and τ_{dir} was calculated at 2 minute temporal resolution (this is hereafter referred to as the 1 m point scale). Output from the 1 m point scale model was spatially averaged to 25 m grid scales and temporally averaged to hourly resolution (hereafter referred to as the 25 m grid scale). To show the difference between synthetic hemispherical image model performance, four model versions were run: 1) unenhanced lidar (L2R-basic), similar to that from Zellweger et al. (2018); 2) enhanced lidar (L2R-enhanced) described in Webster et al. (2020) where trunks and branch points are added to airborne lidar data; 3) a basic version of C2R that doesn't account for τ_{dir} below the horizon line (C2R-basic); and 4) the enhanced C2R (C2R-enhanced) model using a statistical correction for canopy transmissivity. All four models can be run using the Canopy Radiation modelling package CanRad from https://github.com/c-webster/CanRad.jl. τ_{dir} was calculated between 21 December and 22 June and, together with V_f, was multiplied by maximum potential above-canopy shortwave radiation to determine spatial and temporal variability in incoming sub-canopy radiation both across the model domain and between models. Additionally, HPEval (Jonas et al., 2020) was run on two isolated hemispherical photographs taken within a gap and in closed canopy to calculate maximum potential incoming shortwave radiation. The model outputs from the photographs were regarded as "truth".

Model performance using the different hemispherical images was assessed in two steps. The first of these compared isolated synthetic hemispherical images with real hemispherical photographs to understand the relative performance of the different models across entire solar cycles. Second, the performance of the models across spatial and temporal scales was assessed through comparison to L2R-enhanced. Webster et al. (2020) showed this model to be accurate in

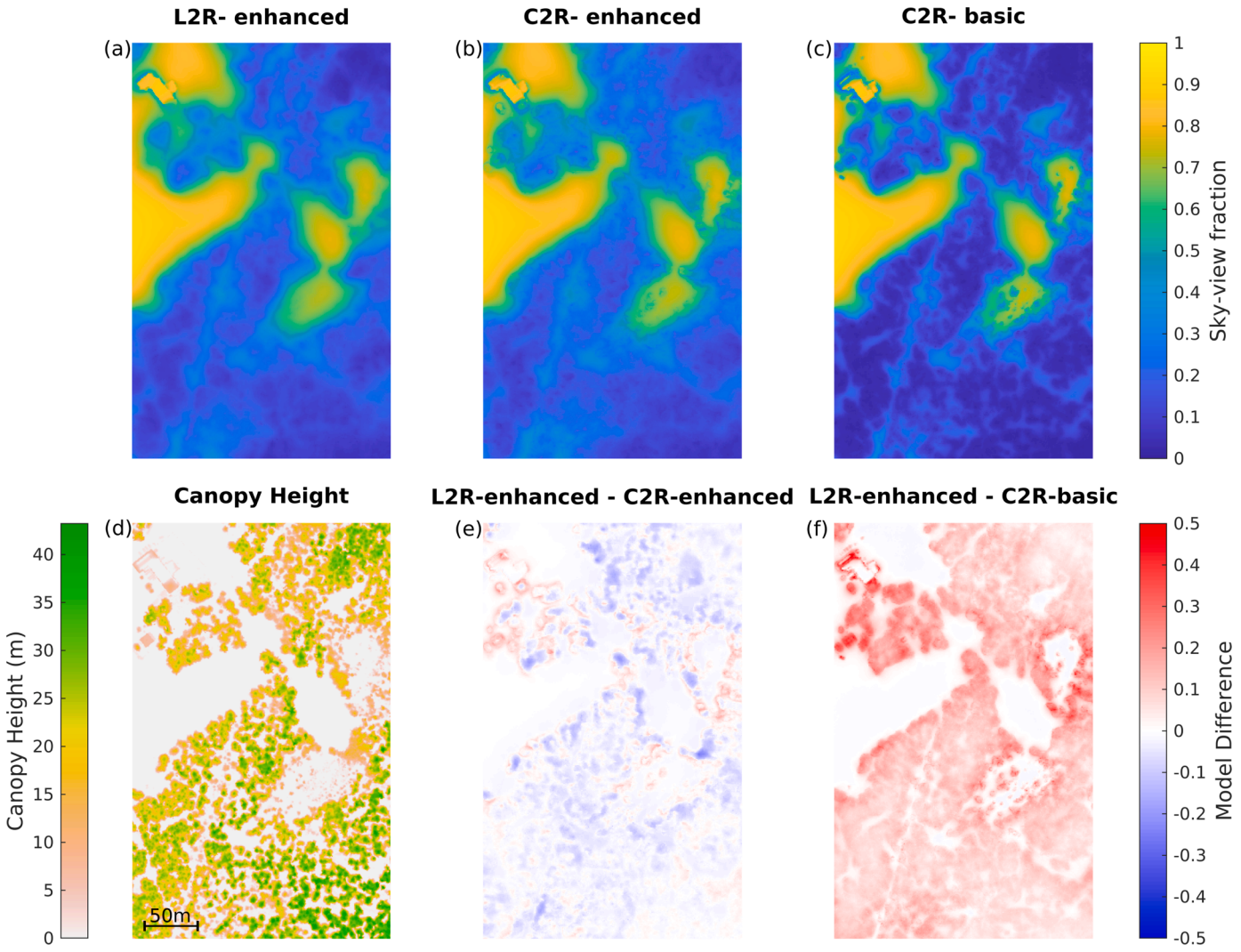

Fig. 3. Sky-view fraction across model domain (300 × 450 m) calculated from the L2R-enhanced (a), C2R-enhanced (b) and C2R-basic (c) models and model difference L2R-ehanced – C2R-enhanced (e) and L2R-enhanced – C2R-basic (f). For reference, canopy structure across model domain is shown in the canopy height model (d).

representing sky-view fraction and incoming radiation at the point scale compared to hemispherical photographs and radiometer measurements. We therefore used this more detailed model to benchmark C2R-enhanced performance across the model domain and time period. Finally, since the goal of C2R-enhanced is to calculate grid-averaged values of V_f and τ_{dir} for potential use in land surface modelling applications, we compared only C2R-enhanced and L2R-enhanced at 25 m grid averages of V_f and τ_{dir}.

4. Results

Both C2R-basic and C2R-enhanced are as capable of representing similar canopy structure controls on the spatial distribution of V_f heterogeneity across the model domain as L2R-enhanced (Fig. 3). Small gaps less than the height of the surrounding canopy are as identifiable in the output from C2R-basic as they are in the two enhanced models. Also, V_f increases away from canopy edges in gaps in all three models. The main difference in model performance between C2R-basic and the two enhanced models is that V_f calculated using the basic model is much lower in all locations directly adjacent to and under canopy (Fig. 3c,f). The exception to this discrepancy between the models is in the denser forests in the north-east and south-east corners of the model domain, where all three models similarly calculate very low V_f values (Fig. 3). In general, however, C2R-basic consistently underestimates V_f across the model domain compared to C2R-enhanced (Fig. 4).

Using L2R-enhanced output as the benchmark, C2R-enhanced better predicts V_f across the model domain compared to C2R-basic. While C2R-basic underestimates V_f at the 1 m scale (Fig. 3f), model differences are more evenly distributed around zero using C2R-enhanced (Fig. 3e). Overall root-mean-square-difference (RMSD) of C2R-enhanced across the model domain at the 1 m point scale (benchmarked to L2R-enhanced) is relatively low (RMSD = 0.04, Fig. 4a) compared to C2R-basic (RMSD = 0.09, Fig. 4c). The differences of C2R-enhanced compared to L2R-enhanced disappear when comparing the average value across 25 m grid cells (Fig. 4b), showing that C2R-enhanced is as capable as L2R-enhanced of representing the average canopy structure in a grid cell. In contrast however, also at the 25 m grid scale, C2R-basic continues to underestimate V_f (Fig. 4d).

The performance of the four synthetic hemispheric image models in estimating shortwave radiation varies compared to the "truth" from hemispherical photographs (Fig. 5). All four models go some way to represent the canopy structure heterogeneity seen in the hemispherical photographs at a dense and small gap site, in particular representing the general shape of the top of the canopy and identifying discontinuities. The largest deviations from the photographs at both locations are by using the two basic models (L2R-basic and C2R-basic). The density of the

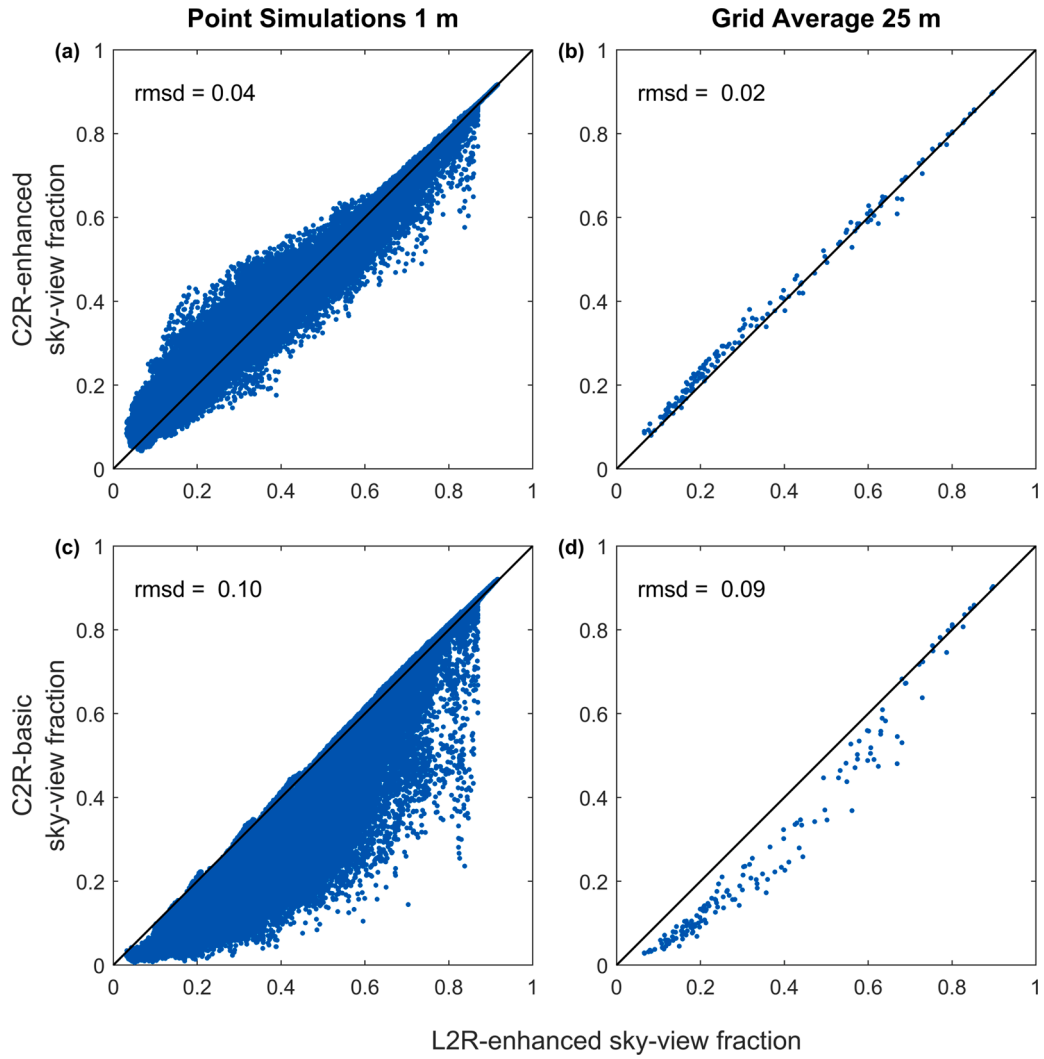

Fig. 4. Difference between L2R-enhanced and C2R-enhanced at 1 m point simulations (a) and across 25 m grid averages (b); difference between L2R-enhanced and C2R-basic at 1 m individual points (c) and 25 m grid averages (d).

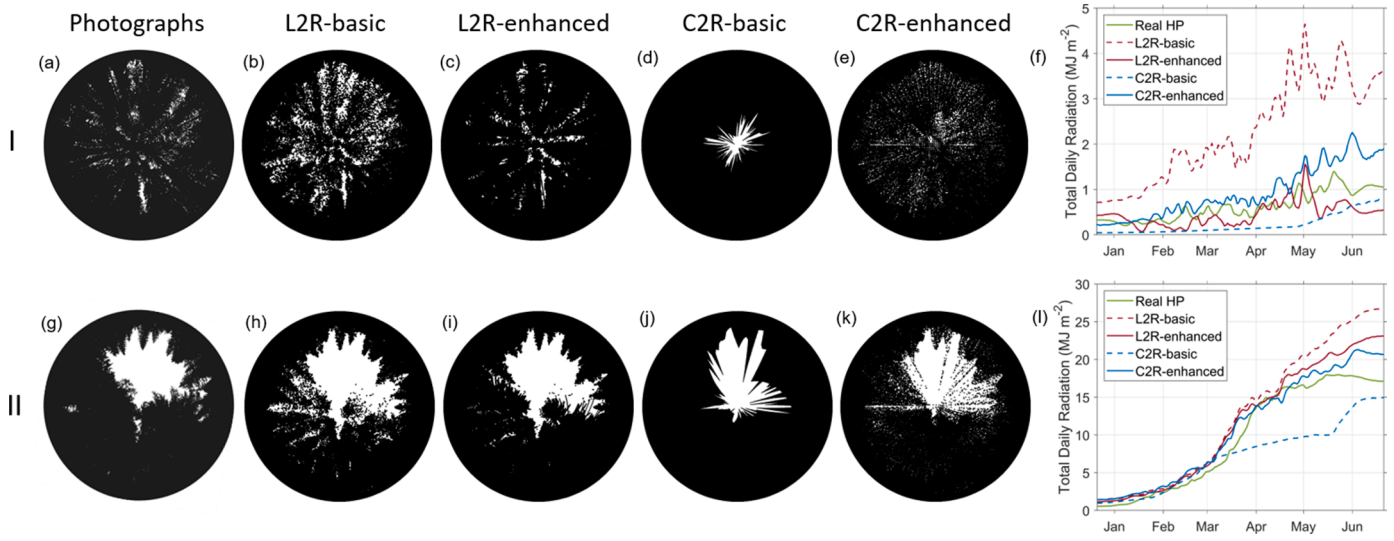

Fig. 5. Hemispherical images from real photographs, and all four synthetic image models at a dense location (I, (a-f)) and at a small gap (II, (g-l)) shown in Fig. 1. Total daily maximum incoming shortwave radiation predicted from each of the hemispherical photographs/images at I (f) and II (l) for each day across a 6-month solar cycle (21 December - 22 June). Hemispherical photographs/images are oriented with south to the top. Note: graphs in (f) and (l) have different scales on y-axis.

original lidar data is too low to accurately represent the true canopy structure and causes an overestimate of total daily incoming shortwave radiation with L2R-basic, which is mitigated by the additional point density created by L2R-enhanced. At the same locations, C2R-basic completely blocks any direct or diffuse radiation below the calculated canopy horizon line (Fig. 5), which results in lower estimates of total daily incoming shortwave radiation compared to the photograph and enhanced models. Additionally, C2R-basic is particularly sensitive to canopy directly overhead – creating spikes in the hemispherical images in areas where no canopy is present in the hemispherical photograph or lidar model versions (Fig. 5g-j). C2R-enhanced goes some way to remove these points, since they are only one pixel thick, thus having a high probability of shortwave transmission. The performance of the two basic models demonstrates that basic canopy information either in 2D or 3D is not adequate to obtain accurate estimates of sub-canopy shortwave radiation and an enhancement of the C2R model is required.

Compared against the photographs ("truth"), both enhanced models (L2R-enhanced and C2R-enhanced) better represent canopy structure variability and estimate total daily shortwave radiation compared to their basic counterparts (Fig. 5). L2R-enhanced performs best, realistically and explicitly representing the individual canopy components in the calculated synthetic hemispherical images, while the canopy representation in the hemispherical images from C2R-enhanced is more generalized. In the dense location (Fig. 5a-f), small gaps between individual trees in the hemispherical photograph are almost explicitly replicated in the synthetic image from L2R-enhanced (Fig. 5c) but not in the image from C2R-enhanced (Fig. 5e). Compared to L2R-enhanced, where gaps between trees are spatially explicit, gaps in the C2R-enhanced hemispherical image are smaller but higher in frequency across the image, reflecting the statistical calculation of the probability of light transmission. The same is true at the small gap location (Fig. 5g-l), where individual tree crowns and trunks are easily identifiable in the photograph (Fig. 5g) and L2R-enhanced image (Fig. 5i), but not in the C2R-enhanced image (Fig. 5k) where canopy structure is more generally represented. The more detailed and explicit canopy representation of L2R-enhanced compared to C2R-enhanced makes it the most suitable for estimating incoming shortwave radiation at meter and minute scales. In particular, L2R-enhanced is most likely to predict instantaneous shortwave radiation at a point due to the physical representation of the canopy.

At coarser temporal resolutions, both enhanced models perform similarly to the photograph model in estimating total daily shortwave radiation across a six-month solar cycle at both locations (Fig. 5f,l). These similar model results demonstrate that general canopy information and representation in synthetic hemispherical images is adequate to produce an accurate estimate for total daily and seasonal incoming shortwave radiation. Both L2R-basic and C2R-basic are inadequate for representation of total shortwave radiation, overestimating and underestimating total incoming shortwave radiation, respectively. The rest of the results therefore focus solely on the relative performance of L2R-enhanced and C2R-enhanced.

At the 1-meter point scale, estimates of τ_{dir} from both L2R-enhanced and C2R-enhanced show both models are capable of representing the same shadow distributions seen in aerial images taken under clear sky conditions (Fig. 6). At this hyper-resolution, L2R-enhanced is better at concretely representing smaller gaps within the forest and light penetration between tree crowns. As well, the boundary between shaded and sun-lit areas is noticeably more distinct in L2R-enhanced compared to C2R-enhanced (Fig. 6b-c compared to f-g). Differences between the two models are both positive and negative and somewhat evenly distributed across the domain, although, not surprisingly, some systematic differences are clustered along canopy edges and in the boundaries of small gaps within the canopy. This pattern of model differences is consistent across the two time periods (i.e. different solar azimuth and zenith angles). Using the L2R-ehanced model as "truth", the RMSD between the two models at both time stamps (0.20 at 9:30 and 0.23 at 12:30; Fig. 5d, h) show the models are not identical in their estimates of τ_{dir}, but, importantly, the mean difference is very low. This demonstrates that although there are large differences between the models in some locations, both models can represent the same average conditions across the flight area.

The relative performance of the two enhanced models in representing the same average shortwave radiation transmission (τ_{dir}) is further demonstrated in Fig. 7, which shows the hourly average incoming shortwave radiation across the whole model domain between 12:00 and 13:00 on June 22 at both 1 m and 25 m scales. Like in Fig. 6, visually

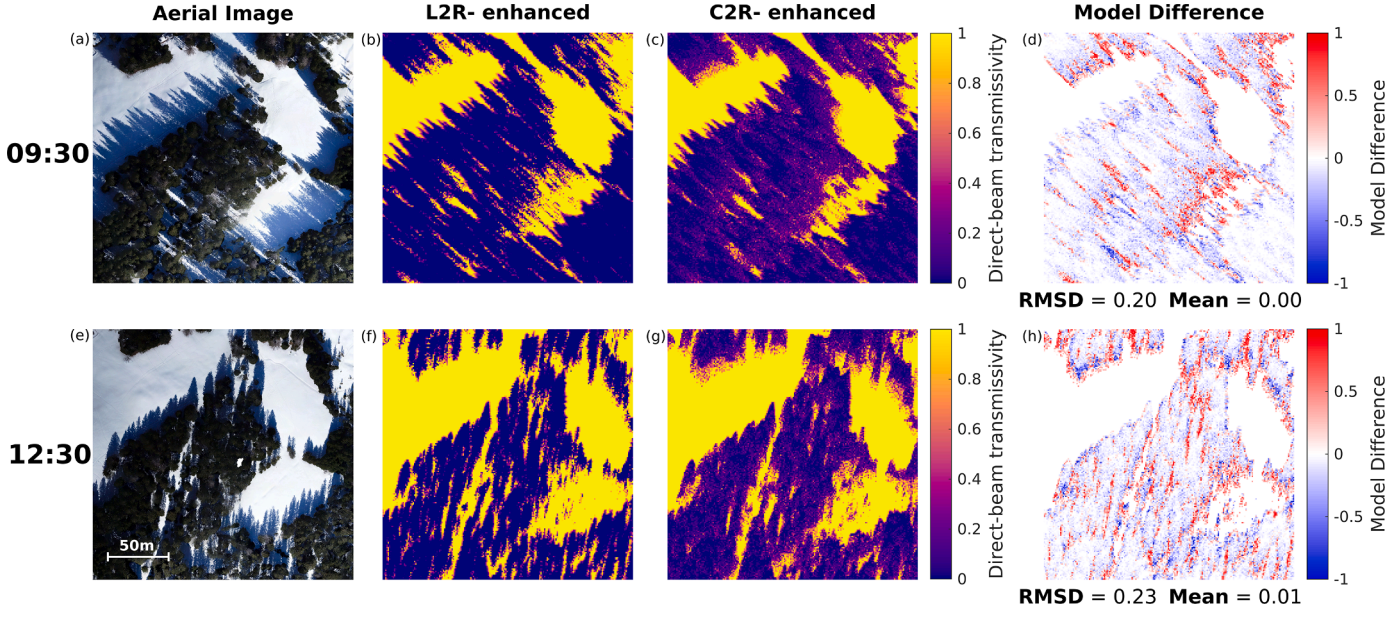

Fig. 6. Aerial images, L2R- and C2R-enhanced model output and difference between the models across flight area (200 × 200 m; Fig. 1) at 09:30 and 12:30 on 28 March 2019. Model output is the calculated values based on the exact solar position at each flight time. In the model difference maps, red = L2R > C2R, blue = L2R < C2R. Predicted shadows in the gap in the south-east quadrant seen in b-c and f-g are not seen in corresponding aerial images (a,e) due to removal of small trees between lidar acquisition and aerial image survey.

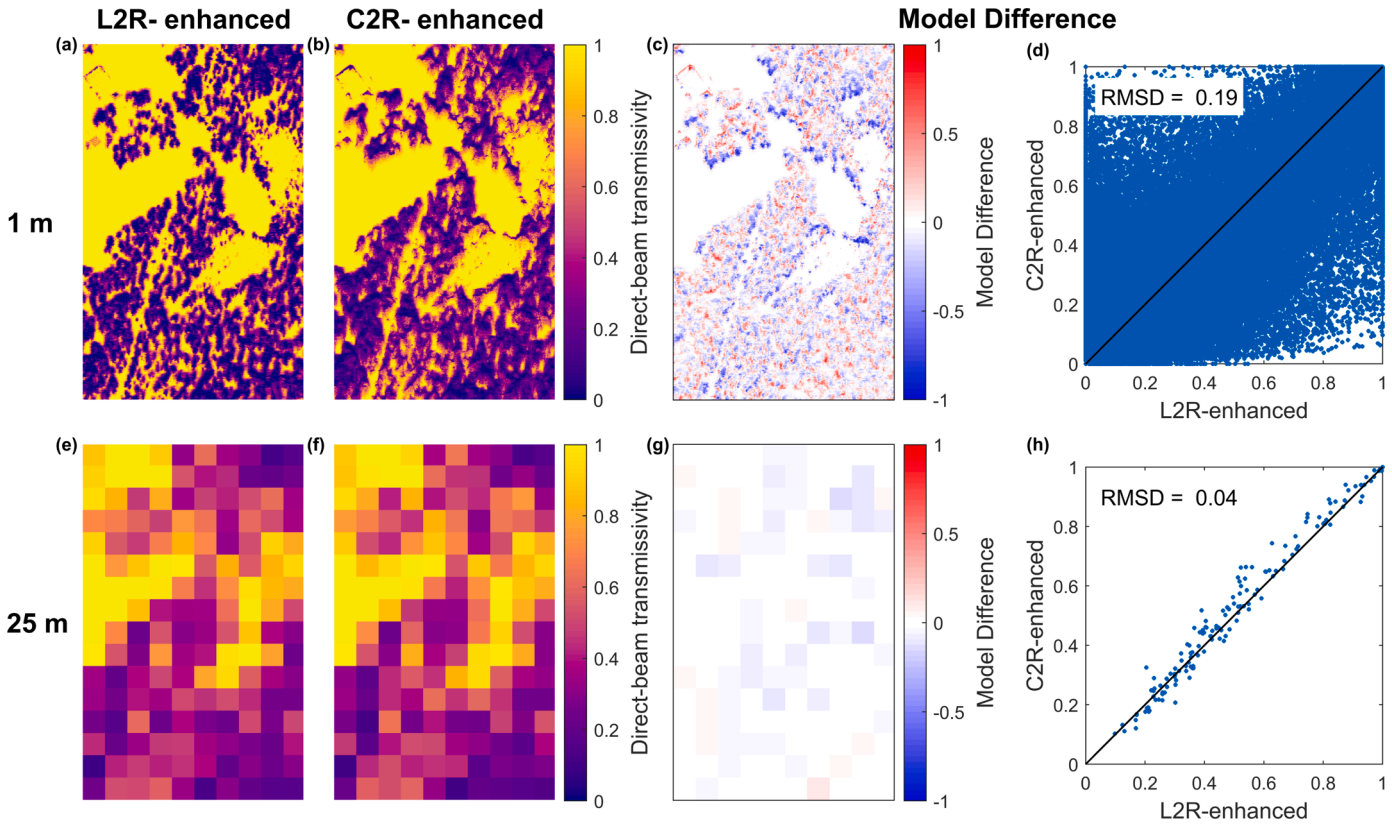

Fig. 7. Average hourly L2R-enhanced and C2R-enhanced model output, model difference across domain (L2R-enhanced – C2R-enhanced) and at individual points (scatterplot) at midday June 22 at 1 m spaced points (a-d) and 25 m grid average (e-h) simulations. Further detail of temporal variability of the model differences can be seen in the three supplementary animations. In the model difference maps (c,g), red = L2R > C2R, blue = L2R < C2R.

both models represent the same heterogeneity in shortwave transmission across the model domain. The hourly average τ_{dir} means both model outputs have blurred boundaries between shaded and sunny areas, compared to only C2R-enhanced output in Fig. 6. The difference map for the 1-meter point scale (Fig. 7c) shows the same seemingly random positive and negative biases are evenly distributed across the domain like in Fig. 6, with concentrations in overestimates of τ_{dir} by C2R-enhanced along sun-exposed edges. Differences between the two models (Fig. 7d) show both positive and negative biases across the full range of τ_{dir} values, and a high RMSD (0.19), similar to the RMSDs at the time of the flights in March. The relatively evenly distributed positive and negative biases across the model domain mean that when model output is averaged to the 25 m grid scale, both models have almost identical grid-averaged values (Fig. 7f-e). RMSD in τ_{dir} between the two models at the 25 m grid average scale is 0.04, substantially lower than the RMSD from the 1 m point scale. These model differences show that even though there are some systematic biases between the two models in isolated locations within the model domain, the generally even distribution of positive and negative biases at the 1 m point scale cancel each other out, resulting in very low average model biases at the grid scale.

The three animations in the supplementary material show how the difference in τ_{dir} between the two enhanced models develops during the day (06:00-20:00) across three days within a 6-month solar cycle (Animation 1 – December 21, winter; Animation 2 - March 28, spring; Animation 3 - June 21, summer), with the statistics summarized in Fig. 8. Model differences are largest between the 1 m outputs, and are highest in summer at lower solar zenith angles (0.19 at zenith angles lower than 30°; Fig. 8c). These larger differences in τ_{dir} at low zenith angles are primarily concentrated along sun-exposed edges (Fig. 7c). Along these edges, there are times when L2R-enhanced estimates higher τ_{dir} (red in

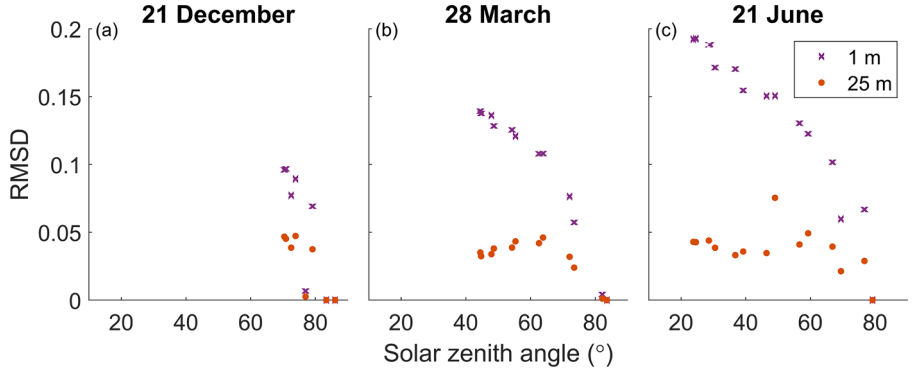

Fig. 8. Relationship between solar zenith angle and model RMSD (between τ_{dir} estimated by L2R-enhanced and C2R-enhanced, using L2R-enhanced as reference) of 1 m spaced points and 25 m grid average on 21 December (a), 28 March (b), and 21 June (c).

difference maps), and other times when C2R-enhanced τ_{dir} values are higher (blue in difference maps). When averaged to the 25 m scale, the larger model errors are reduced across all three days and all zenith angles (Fig. 8). In particular, the maximum RMSD across all three days is 0.07, and only exceeds 0.05 once (16:00 on June 21).

5. Discussion

All four synthetic hemispheric image-based shortwave radiation transmission models can represent some degree of canopy structural heterogeneity across the model domain. The two basic models are too simple in their representation of within-tree crown structure to achieve realistic estimates of V_f (C2R-basic) and τ_{dir} (C2R-basic and L2R-basic), both having systematic biases across the model domain. The poorer performance of L2R-basic compared to the L2R-enhanced model has already been demonstrated by Webster et al. (2020), who showed L2R-basic consistently overestimated τ_{dir} across the model domain due to a lack of lidar point returns in the lower canopy. The poor performance of C2R-basic is also consistent across the model domain due to constant underprediction of V_f and τ_{dir} from a lack of transmissivity below the canopy horizon line. The opposing systematic effects due to the methodological shortcomings in both C2R-basic and L2R-basic demonstrate that estimates of shortwave radiation transfer require accurate and realistic representation of the density of individual tree crowns, whether by realistically representing tree trunks and branches (L2R-enhanced), or correcting for canopy transmissivity by accounting for canopy thickness and species-specific leaf area (C2R-enhanced).

C2R-enhanced provides a next step from the concept initially introduced by Broxton et al. (2015), who corrected for canopy transmissivity below the canopy horizon line using Beer's Law attenuation factor. By incorporating path length, C2R-enhanced can account for the real forest structure in the path of the solar beam to arrive at estimates of τ_{dir} when the sun is below the canopy horizon line. The statistical correction used in C2R-enhanced therefore achieves a more physically-based τ_{dir} estimate, particularly where the solar position is behind small trees, while also allowing τ_{dir} values close to 1 where canopy is thin below the canopy horizon line.

Compared to hemispherical photographs, the two enhanced models perform much better than the basic versions in estimating total daily incoming radiation across a 6-month solar cycle. At higher temporal and spatial resolutions (meter and minute), L2R-enhanced best represented realistic fine scale canopy structure of individual tree crowns due to the explicit tree shape and density contained within lidar data. C2R-enhanced was still able to represent explicit tree shape using the information contained within the canopy height model, but the statistical representation of gaps below the horizon line in the model resulted in meter-to-meter scale discrepancies in the predicted timing and location of sun flecks compared to L2R-enhanced. These differences are because the L2R-enhanced model represents individual trees as distinct individual structures, while C2R-enhanced represents individual trees as structures ranging in low to high probability of shortwave radiation penetration. The L2R-enhanced model can predict exactly where and when light will penetrate the canopy, while C2R-enhanced knows only where light is statistically likely to penetrate the canopy. For example, over the period of one hour as the sun moves between two dense trees, τ_{dir} is almost always 0, except for 10 minutes when it is 1 (the sun is between the two trees). The L2R-enhanced model knows almost exactly when and where the sun-fleck will appear and move on the ground. But C2R-enhanced sees only a smear of canopy with a probability of direct beam transmission of ~0.83, i.e. for 10 minutes of that hour period, τ_{dir} will be 1, but the exact timing is down to statistical randomness (Eq. 5), not physical representation. At the 2-minute resolution, L2R-enhanced will be most accurate, but the 1-hour average will be similar for both models. This is the same reason why, in the difference maps of the 1 m point model outputs, the biases are randomly distributed across the domain. The physically realistic representation of canopy in L2R-enhanced therefore makes it most suitable for hyper-resolution (meter and minute) scale modelling.

Model differences between L2R-enhanced and C2R-enhanced are largest at the 1 m point scale during low solar zenith angles, when the sun position is primarily behind or moving between the tops of tree crowns. Model differences are larger, firstly because at these lower zenith angles the path length through the upper canopy is relatively short and therefore the probability of transmissivity is high, thus model differences will be higher, compared to higher solar zenith angles when the path length through the canopy is longer and transmissivity is lower. Secondly the upper canopy in the synthetic images is much more discontinuous than the lower canopy, and the two models represent the upper canopy slightly differently – L2R-enhanced as spatially explicit tree crowns compared to the less physically realistic shapes resulting from the statistical probability in C2R-enhanced. This different representation does not appear to matter when calculating grid average values, since the larger errors at lower solar zenith angles disappear when the model output was averaged across the 25 m grid cells.

There are some systematic biases between L2R- and C2R-enhanced. The most notable of these is the difference between the two models along sun-exposed edges and up to 5 m into the forest from the edge when solar zenith angle is high (i.e. sun low in the sky). Along these edges, there are times and areas where L2R-enhanced estimates are higher than those from C2R-enhanced, and there are times and areas when the opposite is the case. The reason for these differences is the way each model represents canopy edges and individual trees. C2R-enhanced fills in the canopy from the horizon line to the canopy base, and the model doesn't account for the real tree crown shape. The synthetic hemispheric images from C2R-enhanced represent these areas as filled in with canopy, whereas L2R-enhanced represents the exact structure and shape of individual tree crowns. This "filling in" from C2R-enhanced can therefore lead to under-estimates of shortwave transmission at high solar zenith angles compared to L2R-enhanced. In contrast, C2R-enhanced over-estimates τ_{dir} compared to L2R-enhanced when the solar position is behind thin canopy or individual trees. This is because the statistical model in C2R-enhanced predicts these areas of canopy have high probability of shortwave transmission, but L2R-enhanced is capable of representing small dense tree crowns with low shortwave transmission.

Both enhanced models calculate the same grid-averaged τ_{dir}, and both could therefore theoretically be used to calculate input for land surface models. L2R-enhanced, however, is more computationally intensive than C2R-enhanced. Run grid-by-grid (625 points per grid cell) on an HPC (High Performance Computer), L2R-enhanced required 5 times the calculation time and double the memory per grid compared to C2R-enhanced. Put another way, in the time and memory a computer takes to run one L2R-enhanced grid, it can run 10 grids of C2R-enhanced, and arrive at a similar average across the grid. The use of C2R-enhanced is therefore more suitable for running across large spatial extents for potential use in ecohydrological and land surface modelling applications.

One of the main challenges of C2R-enhanced is the calculation of leaf area for each tree crown. In this study, the simple statistical calculation taken from the literature proved to be sufficient across the model domain, even though it was calculated from Norway Spruce trees in Sweden (Goude et al., 2019). Unfortunately, these sorts of equations are not necessarily available for all tree species nor is it a given that they would be transferable between sites. The availability of information from which to calculate λ values across a field domain could therefore limit application of C2R-enhanced across other sites or larger spatial extents. Additionally, calculation of λ values for each individual tree crown can add to the computation time of the model, requiring segmentation of the CHM. As a sensitivity test, we ran an additional instance of C2R-enhanced using only the domain-averaged λ value for all trees. Although there were differences in the model output between a domain-averaged λ and a tree-specific λ, the performance of the

domain-averaged λ version compared to the L2R-enhanced model remained the same as the tree-specific λ version shown in Figs. 3-7. It is therefore possible that a single λ value that describes the general density of tree crowns is all that would be required as model input, with potential added detail by providing different values for different species if such information was available. The results from this sensitivity test as well as from the main analysis highlight the importance of validating the C2R-enhanced model, ideally by comparison to the L2R-enhanced model where high-resolution lidar data is available, or by comparison to real hemispherical photographs.

C2R-enhanced used a CHM that was calculated from airborne lidar data with a resolution of 42 points/m^2, which is relatively high for such a dataset. Given that the only requirement of the CHM is that it represents individual tree crowns, C2R-enhanced could also be applied to CHMs calculated from airborne lidar data that is closer to 1-2 points/m^2, the scale of many catchment- and nation-wide datasets. Lidar processing tools such as Lastools (https://rapidlasso.com/), have settings that allow you to increase the virtual size of the lidar points, removing gaps in individual tree crowns in the final CHM that would otherwise result from sparse lidar point clouds. These sorts of tools mean it is possible to run C2R-enhanced using lower resolution airborne lidar data. Large-scale datasets at this resolution are becoming common-place, thus the potential for application of C2R-enhanced is only increasing.

Finally, the ability of C2R-enhanced to calculate canopy shortwave radiation transmissivity over spatial extents > 100 km^2 creates new possibilities for research applications at previously impossible scales. Given output from C2R-enhanced follows the same structure as L2R-enhanced, which has already been used to improve estimates of snow cover and ablation in forests at gridded scales (Mazzotti et al., 2021), C2R-enhanced can now be used within forest energy balance and eco-hydrological models both within research and operational frameworks. For example, including before and after forest structure scenarios following forest disturbance (e.g. wildfire or windthrow) or implementation of management strategies would improve understanding of how these affect streamflow (Harpold et al., 2014; Currier et al., 2022) or forest microclimate and subsequent habitat suitability and species biodiversity (Zellweger et al., 2020). Since most forest disturbances create highly heterogeneous forest structure, radiation transfer models that can accurately and efficiently represent these changes are required to fully understand the ecohydrological implications of these land surface changes. Furthermore, incorporating explicit forest structure within snow and hydrological models will enable improvements in estimates of snow cover as well as melt contributions to streamflow (Broxton et al., 2021). Finally, explicit representation of topographic and snow surface shading across landscapes by C2R-enhanced create the potential to better understand how shading affects simulated wintertime land surface albedo (Webster and Jonas, 2018; Malle et al, 2021). There is therefore tremendous potential for incorporating these new modelling tools to include tree-scale forest structure effects within larger-scale ecological and hydrological applications.

6. Conclusion

This study demonstrated that accurate 25 m grid scale estimates of canopy shortwave direct and diffuse transmissivity can be obtained using only information contained within a canopy height model. The model CanopyHeightModel2Radation (C2R) calculates direct beam transmissivity based on the geometric arrangement of the surrounding canopy (C2R-basic), while improving on the C2R-basic version by applying a statistical correction for the canopy transmissivity using canopy thickness and species-specific leaf area to determine the probability of light transmission across the hemispherical view (C2R-enhanced). Performance of C2R-enhanced at the point and grid scales was assessed against the enhanced version of Lidar2Radiation model (L2R-enhanced), which represents canopy structure by adding trunks and branches within tree crowns to existing airborne lidar data. The explicit canopy density information within both L2R-enhanced and C2R-enhanced means both models resolve the complex variability in shortwave radiation transmission when the solar position is below the canopy horizon line. Differences between the two enhanced models, measured by calculating RMSD, are relatively high (0.17) at 1 m and 10-minute resolution due to the different representations of canopy structure between the two models. These high-resolution differences occur because C2R-enhanced has a physical representation of the top of the canopy but uses a statistical approach to calculate transmissivity. In contrast, L2R-enhanced uses a physical representation of tree crown, trunk and branch position based on information available from the lidar data. The difference in estimates between the two enhanced models is reduced to an RMSD between 0.01 and 0.07 when the model outputs are averaged over hourly and 25 × 25 m grid scales across a 6-month solar cycle between the winter and summer solstices. Both models therefore arrive at similar grid- and hourly-averaged estimates, but C2R-enhanced requires simpler input datasets and fewer computational resources. Based on the relative performance between the two enhanced models, it is recommended that the physically explicit representation in L2R-enhanced is used when estimating canopy transmissivity at high spatial and temporal (meter and minute) resolutions, while C2R-enhanced is used when computing shortwave transmissivity across large spatial scales where average values within grid cells are required, for example as input into forest energy balance models. Obtaining output from C2R-enhanced across landscapes and incorporating into existing forest energy balance models creates exciting opportunities for investigating forest structure controls on forest hydrology and ecosystems across previously impossible spatial extents.

Declaration of Competing Interest

The authors declare that they have no known competing financial interests or personal relationships that could have appeared to influence the work reported in this paper.

Data availability

The four synthetic hemispheric image based models used in this paper are available as part of the canopy radiation modelling package CanRad at https://github.com/c-webster/CanRad.jl

Acknowledgements

The authors would like to thank Lucie Eberhard (WSL/SLF) for the aerial images used in Fig. 6. Clare Webster received support from the Swiss National Science Foundation (SNF, project P2SKP2_178173).

Supplementary materials

Supplementary material associated with this article can be found, in the online version, at doi:10.1016/j.agrformet.2023.109429.

References

Baldocchi, D.D., Law, B.E., Anthoni, P.M., 2000. On measuring and modeling energy fluxes above the floor of a homogeneous and heterogeneous conifer forest. Agricultural and Forest Meteorology 102 (2-3), 187–206. https://doi.org/10.1016/S0168-1923(00)00098-8.

Bales, R.C., Hopmans, J.W., O'Geen, A.T., Meadows, M., Hartsough, P.C., Kirchner, P., Hunsaker, C.T., Beaudette, D., 2011. Soil moisture response to snowmelt and rainfall in a Sierra Nevada mixed-conifer forest. Vadose Zone Journal 10 (3), 786–799. https://doi.org/10.2136/vzj2011.0001.

Bartlett, P.A., MacKay, M.D., Verseghy, D.L., 2006. Modified snow algorithms in the Canadian land surface scheme: Model runs and sensitivity analysis at three boreal forest stands. Atmosphere-Ocean 44 (3), 207–222. https://doi.org/10.3137/ao.440301.

Bode, C.A., Limm, M.P., Power, M.E., Finlay, J.C., 2014. Subcanopy Solar Radiation model: Predicting solar radiation across a heavily vegetated landscape using LiDAR

and GIS solar radiation models. Remote Sensing of Environment 154, 387–397. https://doi.org/10.1016/j.rse.2014.01.028.
Broxton, P.D., Harpold, A.A., Biederman, J.A., Troch, P.A., Molotch, N.P., Brooks, P.D., 2015. Quantifying the effects of vegetation structure on snow accumulation and ablation in mixed-conifer forests. Ecohydrology 8 (6), 1073–1094. https://doi.org/10.1002/eco.1565.
Broxton, P.D., Moeser, C.D., Harpold, A., 2021. Accounting for Fine-Scale Forest Structure is Necessary to Model Snowpack Mass and Energy Budgets in Montane Forests. Water Resources Research 57 (12), e2021WR029716. https://doi.org/10.1029/2021WR029716.
Clark, M.P., Nijssen, B., Lundquist, J.D., Kavetski, D., Rupp, D.E., Woods, R.A., Freer, J. E., Gutmann, E.D., Wood, A.W., Gochis, D.J., Rasmussen, R.M., Tarboton, D.G., Mahat, V., Flerchinger, G.N., Marks, D.G., 2015. A unified approach for process-based hydrologic modelling: 2. Model implementation and case studies. Water Resources Research 51 (4), 2515–2542. https://doi.org/10.1002/2015WR017198.
Currier, W.R., Pflug, J., Mazzotti, G., Jonas, T., Deems, J.S., Bormann, K.J., Painter, T.H., Hiemstra, C.A., Gelvin, A., Uhlmann, Z., Spaete, L., 2019. Comparing aerial lidar observations with terrestrial lidar and snow-probe transects from NASA's 2017 SnowEx campaign. Water Resources Research 55 (7), 6285–6294. https://doi.org/10.1029/2018WR024533.
Currier, W.R., Sun, N., Wigmosta, M., Cristea, N., Lundquist, J.D., 2022. The impact of forest-controlled snow variability on late-season streamflow varies by climatic region and forest structure. Hydrological Processes, e14614. https://doi.org/10.1002/hyp.14614.
Dalponte, M., Coomes, D.A., 2016. Tree-centric mapping of forest carbon density from airborne laser scanning and hyperspectral data. Methods in ecology and evolution 7 (10), 1236–1245. https://doi.org/10.1111/2041-210X.12575.
Erbs, D.G., Klein, S.A., Duffie, J.A., 1982. Estimation of the diffuse radiation fraction for hourly, daily and monthly-average global radiation. Solar energy 28 (4), 293–302. https://doi.org/10.1016/0038-092X(82)90302-4.
Essery, R., Bunting, P., Rowlands, A., Rutter, N., Hardy, J., Melloh, R., Link, T., Marks, D., Pomeroy, J., 2008a. Radiative transfer modeling of a coniferous canopy characterized by airborne remote sensing. Journal of Hydrometeorology 9 (2), 228–241. https://doi.org/10.1175/2007JHM870.1.
Essery, R., Pomeroy, J., Ellis, C., Link, T., 2008b. Modelling longwave radiation to snow beneath forest canopies using hemispherical photography or linear regression. Hydrological Processes: An International Journal 22 (15), 2788–2800. https://doi.org/10.1002/hyp.6930.
Ferraz, A., Saatchi, S., Bormann, K.J., Painter, T.H., 2018. Fusion of NASA Airborne Snow Observatory (ASO) lidar time series over mountain forest landscapes. Remote Sensing 10 (2), 164. https://doi.org/10.3390/rs10020164.
Ginzler, C., Hobi, M.L., 2015. Countrywide stereo-image matching for updating digital surface models in the framework of the Swiss National Forest Inventory. Remote Sensing 7 (4), 4343–4370. https://doi.org/10.3390/rs70404343.
Goude, M., Nilsson, U., Holmström, E., 2019. Comparing direct and indirect leaf area measurements for Scots pine and Norway spruce plantations in Sweden. European Journal of Forest Research 138 (6), 1033–1047. https://doi.org/10.1007/s10342-019-01221-2.
Hardy, J.P., Melloh, R., Koenig, G., Marks, D., Winstral, A., Pomeroy, J.W., Link, T., 2004. Solar radiation transmission through conifer canopies. Agricultural and forest meteorology 126 (3-4), 257–270. https://doi.org/10.1016/j.agrformet.2004.06.012.
Harpold, A.A., Biederman, J.A., Condon, K., Merino, M., Korgaonkar, Y., Nan, T., Sloat, L.L., Ross, M., Brooks, P.D., 2014. Changes in snow accumulation and ablation following the Las Conchas Forest Fire, New Mexico, USA. Ecohydrology 7 (2), 440–452. https://doi.org/10.1002/eco.1363.
Jonas, T., Webster, C., Mazzotti, G., Malle, J., 2020. HPEval: A canopy shortwave radiation transmission model using high-resolution hemispherical images. Agricultural and Forest Meteorology 284, 107903. https://doi.org/10.1016/j.agrformet.2020.107903.
Jucker, T., Caspersen, J., Chave, J., Antin, C., Barbier, N., Bongers, F., Dalponte, M., van Ewijk, K.Y., Forrester, D.I., Haeni, M., Higgins, S.I., 2017. Allometric equations for integrating remote sensing imagery into forest monitoring programmes. Global change biology 23 (1), 177–190. https://doi.org/10.1111/gcb.13388.
Khosravipour, A., Skidmore, A.K., Isenburg, M., Wang, T., Hussin, Y.A., 2014. Generating pit-free canopy height models from airborne lidar. Photogrammetric Engineering & Remote Sensing 80 (9), 863–872. https://doi.org/10.14358/PERS.80.9.863.
Kükenbrink, D., Schneider, F.D., Schmid, B., Gastellu-Etchegorry, J.P., Schaepman, M.E., Morsdorf, F., 2021. Modelling of three-dimensional, diurnal light extinction in two contrasting forests. Agricultural and Forest Meteorology 296, 108230. https://doi.org/10.1016/j.agrformet.2020.108230.
Lawrence, D.M., Fisher, R.A., Koven, C.D., Oleson, K.W., Swenson, S.C., Bonan, G., Collier, N., Ghimire, B., Kampenhout, L., Kennedy, D., Kluzek, E., Lawrence, P.J., Li, F., Li, H., Lombardozzi, D., Riley, W.J., Sacks, W.J., Shi, M., Vertenstein, M., Zeng, X., 2019. The community land model version 5: Description of new features, benchmarking, and impact of forcing uncertainty. Journal of Advances in Modelling Earth Systems 11 (12), 4245–4287. https://doi.org/10.1029/2018MS001583.
Malle, J., Rutter, N., Mazzotti, G., Jonas, T., 2019. Shading by trees and fractional snow cover control the subcanopy radiation budget. Journal of Geophysical Research: Atmospheres 124 (6), 3195–3207. https://doi.org/10.1029/2018JD029908.
Malle, J., Rutter, N., Webster, C., Mazzotti, G., Wake, L., Jonas, T., 2021. Effect of forest canopy structure on wintertime land surface Albedo: evaluating CLM5 simulations with in-situ measurements. Journal of Geophysical Research: Atmospheres 126 (9), e2020JD034118. https://doi.org/10.1029/2020JD034118.
Mazzotti, G., Malle, J., Barr, S., Jonas, T., 2019. Spatially continuous characterization of forest canopy structure and subcanopy irradiance derived from handheld radiometer surveys. Journal of Hydrometeorology 20 (7), 1417–1433. https://doi.org/10.1175/JHM-D-18-0158.1.
Mazzotti, G., Essery, R., Webster, C., Malle, J., Jonas, T., 2020. Process-level evaluation of a hyper-resolution forest snow model using distributed multisensor observations. Water Resources Research 56 (9), e2020WR027572. https://doi.org/10.1029/2020WR027572.
Mazzotti, G., Webster, C., Essery, R., Jonas, T., 2021. Increasing the Physical Representation of Forest-Snow Processes in Coarse-Resolution Models: Lessons Learned From Upscaling Hyper-Resolution Simulations. Water Resources Research 57 (5), e2020WR029064. https://doi.org/10.1029/2020WR029064.
Moeser, D., Roubinek, J., Schleppi, P., Morsdorf, F., Jonas, T., 2014. Canopy closure, LAI and radiation transfer from airborne LiDAR synthetic images. Agricultural and Forest Meteorology 197, 158–168. https://doi.org/10.1016/j.agrformet.2014.06.008.
Mohan, M., Silva, C.A., Klauberg, C., Jat, P., Catts, G., Cardil, A., Hudak, A.T., Dia, M., 2017. Individual tree detection from unmanned aerial vehicle (UAV) derived canopy height model in an open canopy mixed conifer forest. Forests 8 (9), 340. https://doi.org/10.3390/f8090340.
Musselman, K.N., Molotch, N.P., Margulis, S.A., Kirchner, P.B., Bales, R.C., 2012a. Influence of canopy structure and direct beam solar irradiance on snowmelt rates in a mixed conifer forest. Agricultural and Forest Meteorology 161, 46–56. https://doi.org/10.1016/j.agrformet.2012.03.011.
Musselman, K.N., Molotch, N.P., Margulis, S.A., Lehning, M., Gustafsson, D., 2012b. Improved snowmelt simulations with a canopy model forced with photo-derived direct beam canopy transmissivity. Water Resources Research 48 (10). https://doi.org/10.1029/2012WR012285.
Musselman, K.N., Margulis, S.A., Molotch, N.P., 2013. Estimation of solar direct beam transmittance of conifer canopies from airborne LiDAR. Remote Sensing of Environment 136, 402–415. https://doi.org/10.1016/j.rse.2013.05.021.
National Land Survey of Finland, 2019. Laser scanning data [WWW Document]. URL=. https://www.maanmittauslaitos.fi/en/maps-and-spatial-data/expert-users/product-descriptions/laser-scanning-data. accessed 30 June 2022.
NOAA, 2005. Solar Calculation Details [WWW Document]. URL=. https://www.esrl.noaa.gov/gmd/grad/solcalc/calcdetails.html. accessed 29 May 2018.
Nilson, T., 1971. A theoretical analysis of the frequency of gaps in plant stands. Agricultural meteorology 8, 25–38. https://doi.org/10.1016/0002-1571(71)90092-6.
Piermattei, L., Marty, M., Karel, W., Ressl, C., Hollaus, M., Ginzler, C., Pfeifer, N., 2018. Impact of the acquisition geometry of very high-resolution Pléiades imagery on the accuracy of canopy height models over forested alpine regions. Remote Sensing 10 (10), 1542. https://doi.org/10.3390/rs10101542.
Price, M.A., 1997. MS thesis. Dept. of Mathematics, Oregon State University.
Swisstopo, 2017. LiDAR data acquisition [WWW Document]. URL=. https://www.swisstopo.admin.ch/en/knowledge-facts/geoinformation/lidar-data.html. accessed 30 June 2022.
Webster, C., Jonas, T., 2018. Influence of canopy shading and snow coverage on effective albedo in a snow-dominated evergreen needleleaf forest. Remote Sensing of Environment 214, 48–58. https://doi.org/10.1016/j.rse.2018.05.023.
Webster, C., Mazzotti, G., Essery, R., Jonas, T., 2020. Enhancing airborne LiDAR data for improved forest structure representation in shortwave transmission models. Remote Sensing of Environment 249, 112017. https://doi.org/10.1016/j.rse.2020.112017.
Zellweger, F., Baltensweiler, A., Schleppi, P., Huber, M., Küchler, M., Ginzler, C., Jonas, T., 2019. Estimating below-canopy light regimes using airborne laser scanning: An application to plant community analysis. Ecol. Evol. 9, 9149–9159. https://doi.org/10.1002/ece3.5462.
Zellweger, F., De Frenne, P., Lenoir, J., Vangansbeke, P., Verheyen, K., Bernhardt-Römermann, M., Baeten, L., Hédl, R., Berki, I., Brunet, J., Van Calster, H., 2020. Forest microclimate dynamics drive plant responses to warming. Science 368 (6492), 772–775. https://doi.org/10.1126/science.aba6880.
Zörner, J., Dymond, J., Shepherd, J., Jolly, B., 2018. Pycrown-Fast raster-based individual tree segmentation for LIDAR data. Landcare Research Ltd, Lincoln, New Zealand. https://doi.org/10.7931/M0SR-DN55.